ARTICLES
https://doi.org/10.1038/s41567-018-0242-5
nature physics

Precision spectroscopy of helium in a magic wavelength optical dipole trap

R. J. Rengelink[1], Y. van der Werf[1], R. P. M. J. W. Notermans[1,3], R. Jannin[1], K. S. E. Eikema[1], M. D. Hoogerland[2] and W. Vassen[1*]

Improvements in both theory and frequency metrology of few-electron systems such as hydrogen and helium have enabled increasingly sensitive tests of quantum electrodynamics, as well as ever more accurate determinations of fundamental constants and the size of the nucleus. At the same time, advances in cooling and trapping of neutral atoms have revolutionized the development of increasingly accurate atomic clocks. Here, we combine these fields to reach very high precision on an optical transition in the helium atom by employing a ^{4}He Bose–Einstein condensate confined in a magic wavelength optical dipole trap. The measured transition accurately connects the ortho- and parastates of helium and constitutes a stringent test of quantum electrodynamics theory. In addition, we test polarizability calculations and ultracold scattering properties of the helium atom. Finally, our measurement lays the foundation for a determination of the ^{3}He–^{4}He nuclear charge radius difference with an accuracy exceeding that of muonic helium measurements currently being performed in the context of the proton radius puzzle.

In recent decades, high-precision spectroscopy measurements in atomic-physics-scale systems have pushed precision tests of quantum electrodynamics (QED), one of the cornerstones of the standard model of physics, ever further[1,2] and have led to accurate determinations of fundamental constants[3–6]. However, recent measurements of transition frequencies in muonic hydrogen have revealed a discrepancy of six standard deviations[7,8] with respect to the accepted Committee on Data for Science and Technology (CODATA) value for the proton charge radius. This discrepancy, which has become known as the proton radius puzzle, has stimulated strong interest in the field, as its confirmation implies the violation of lepton universality, one of the pillars of the standard model. New experiments in atomic hydrogen[9,10] and muonic deuterium[11] have not solved the puzzle, prompting research into other elements such as muonic helium[12]. From these measurements the charge radii of the alpha-particle and the helion (1.68 and 1.97 fm, respectively) are projected to be determined with sub-attometre accuracy, which should be compared to high-precision experiments in electronic helium atoms or ions.

QED theory of the helium atom, which with two electrons is more complicated than hydrogen, has seen impressive improvements in recent years, with QED corrections up to order $m\alpha^6$ (with m the electron mass and α the fine structure constant) now evaluated[2]. Recent experiments are in good agreement[13–20] and may allow a competitive value for the fine structure constant in the near future[21–24]. The anticipated evaluation of the next highest order corrections[2] ($m\alpha^7$) would allow the determination of the ^{4}He nuclear charge radius with an accuracy better than 1%. At present, nuclear charge radii can already be determined differentially—that is, with respect to ^{4}He—due to cancellation of higher-order terms in the isotope shift. Using this approach, the radii of the exotic halo nuclei ^{6}He and ^{8}He (refs [25,26]), as well as the stable isotope ^{3}He (refs [27–29]) were determined with accuracies far exceeding electron scattering experiments[30]. However, different experiments on the ^{3}He–^{4}He isotope shift show significant discrepancies[2], even between different measurements of the same dipole-allowed $2\,^3S_1 \rightarrow 2\,^3P$ transition[19]. Furthermore, improving the experimental accuracy on this transition is challenging due to the 1.6 MHz natural linewidth and the presence of quantum interference shifts[24]. Only one previous experiment has used the doubly forbidden $2\,^3S_1 \rightarrow 2\,^1S_0$ transition[29], which in contrast has an excellent quality factor of 2.4×10^{13} (natural linewidth 8 Hz) that poses no fundamental limit in the foreseeable future.

Here we report a new measurement of the $2\,^3S_1 \rightarrow 2\,^1S_0$ transition frequency at 1,557 nm that improves the previous result by an order of magnitude ($\delta\nu/\nu = 1.0\times10^{-12}$). Our measurement has been performed using a Bose–Einstein condensate (BEC) in the metastable $2\,^3S_1$ state confined in an optical dipole trap (ODT) at a previously predicted[31] magic wavelength for this transition. At such a magic wavelength the a.c. Stark shift on the transition vanishes, a property that has been exploited to realize atomic clocks operating at a stability in the 10^{-19} region[32,33], allowing constraints on a possible time-variation of fundamental constants[34]. Moreover, ab initio calculations of polarizability have recently emerged as an alternative means of testing atomic theory at a level sensitive to QED effects[35–37]. By fine-tuning the ODT laser wavelength to reduce the a.c. Stark shift on the transition frequency, we measure the magic wavelength to high accuracy, providing a stringent test for ab-initio calculations[38].

Our approach has also enabled us to measure the mean-field, or cold-collision, shift on the transition by direct observation. This frequency shift was instrumental in the first observation of Bose–Einstein condensation of atomic hydrogen via two-photon excitation of the $1S \rightarrow 2S$ transition, where the enormous density of the BEC gave rise to a huge mean-field shift[39,40]. The associated transition lineshape allowed quantitative analysis of these results[41]. In earlier work[42], we showed how this lineshape is affected by an asymmetry in the trapping potential for $2\,^3S_1$ and $2\,^1S_0$ atoms, and we could extract the $2\,^1S_0$–$2\,^3S_1$ scattering length with 50% accuracy. Now, working in a magic wavelength trap, we are able to improve this accuracy by an order of magnitude.

[1]LaserLaB, Department of Physics and Astronomy, Vrije Universiteit, Amsterdam, the Netherlands. [2]Dodd-Walls Centre for Photonic and Quantum Technologies, Department of Physics, University of Auckland, Auckland, New Zealand. [3]Present address: Department of Physics, Stanford University, Stanford, CA, USA. *e-mail: w.vassen@vu.nl

These measurements therefore test our knowledge of the helium atom in three different ways. The transition frequency measured here is a test of level energies and is sensitive to the finite size of the nucleus. The magic wavelength determination is a precision test of atomic structure as a whole, and is therefore also sensitive to transition dipole moments. Finally, the scattering length derived from the mean-field shift is a precise test of the molecular potentials between helium atoms.

Set-up

We prepare a BEC of typically 10^6 atoms in the metastable $2\,^3S_1$ state[29] (19.82 eV above the $1\,^1S_0$ ground state, lifetime ~8,000 s; ref. [14]), and transfer it into a dipole trap at 319.8 nm. The atoms are spin-polarized in the spin-stretched $m_J=+1$ magnetic substate so that ionization via two-body collisions (Penning ionization) is strongly suppressed[43]. Figure 1a shows the geometry of the dipole trap. A tightly focused ODT beam is passed through the vacuum chamber, then refocused and passed through the chamber again with orthogonal linear polarization, intersecting itself at an angle of 19°. The atoms are trapped at the intersection, where the probe laser is applied counterpropagating with respect to the incident ODT beam. To detect excitation of the transition, we measure the increased Penning ionization rate from the excited $2\,^1S_0$ atoms using a microchannel plate detector (MCP) and counter (see Methods). This detection method provides a substantially better signal-to-noise ratio compared to a signal based on the loss of $2\,^3S_1$ atoms as used previously[17,29,42]. After excitation, the remaining atoms (>90%) are dropped under gravity onto another MCP detector placed 17 cm directly below the trap, producing a time-of-flight signal. From a bimodal fit to the time-of-flight signal, we determine the chemical potential and atom number of the BEC, as well as the temperature and atom number of the thermal cloud.

Figure 1b shows the optical set-up generating the probe and ODT laser light. Part of the probe laser light is also amplified and mixed with a second independent laser to generate the ODT light. This second laser is monitored by a high-resolution wavemeter to determine the ODT laser wavelength (see Methods). The optical and electronic set-up for generating the probe and ODT laser light are described in refs [42,44].

To account for the Zeeman shift arising from the ambient magnetic field in the laboratory (that is, Earth's magnetic field), we alternate between exciting from the $m_J=+1$ and $m_J=-1$ states (see Methods), which have first-order Zeeman shifts of equal magnitude but opposite sign. Exciting from the $m_J=0$ state, which shows no first-order Zeeman shift, is not possible due to a high Penning ionization rate[43]. Every measurement is alternated with a background measurement to monitor the level of background ion counts. In this way, we build up a double-peak spectrum, as shown in Fig. 2. We fit each measured line with two Gaussian peaks (see Methods) and calculate the centre frequencies.

Results

By employing a magic wavelength ODT, the a.c. Stark shift induced by the trap is greatly reduced compared to previous work[29]. At the start of our measurements the magic wavelength was not yet known with sufficient accuracy to eliminate the a.c. Stark shift completely, and a residual trap-induced a.c. Stark shift remains as a systematic shift that needs to be calibrated. In addition to this, two other systematic shifts are present that contribute roughly equally to the final accuracy: the a.c. Stark shift from the probe laser, and the mean-field shift, which is proportional to the chemical potential of the BEC.

To account for these systematics we performed multiple measurements in which we varied the ODT and probe laser powers as well as the chemical potential of the BEC. Since all of these systematic shifts are linear with respect to their corresponding experimental observable, we can fit the data with a multiple linear regression model, as shown in Fig. 3. From this model we extracted the transition frequency as well as the slopes of the a.c. Stark shifts and the mean-field shift simultaneously. For every measurement week, a single complete fit of the regression model was performed, in which the total number of measured transition frequencies varied between 16 and 39.

It was experimentally not possible to vary all parameters independently. In particular, the ODT power and chemical potential are highly correlated because a deeper trap is better able to hold a high

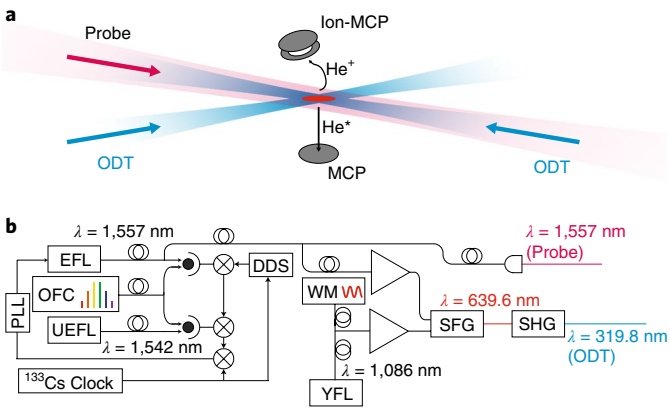

Fig. 1 | Description of the experimental set-up. a, Schematic of the experimental geometry. Two overlapping laser beams crossing at an angle of 19° form the ODT. The probe light is counterpropagating with respect to one of the ODT beams. A high-voltage biased MCP detector above the set-up detects He^+ ions generated by excited atoms. A grounded MCP below the set-up detects the remaining metastable atoms (He^*) that fall under gravity when they are released from the trap. **b**, Schematic of the laser set-up. An erbium fibre laser (EFL) is transfer-locked in a phase-locked loop (PLL) to an ultrastable erbium fibre laser (UEFL) via an optical frequency comb (OFC). Control over the frequency offset is provided by an in-loop direct digital synthesizer (DDS). The EFL serves as the probe laser, but part of it is also split off to seed a fibre amplifier. An independent ytterbium fibre laser (YFL) is amplified and overlapped with this light to generate the sum frequency (SFG), which is frequency-doubled in a second-harmonic generation (SHG) stage. A wavemeter (WM) is used to measure the wavelength of the YFL.

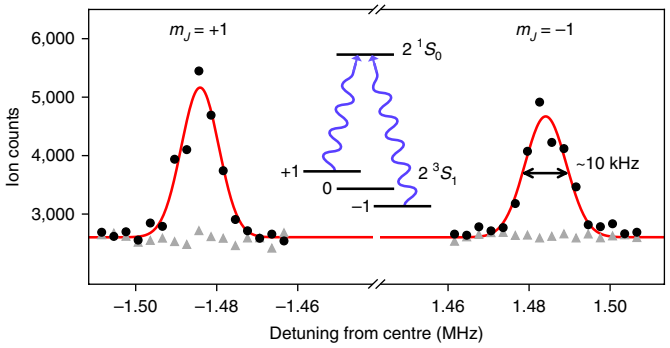

Fig. 2 | A typical spectroscopy scan. Each black circle indicates the signal from a single run of the experiment when spectroscopy light is applied. The grey triangles are background calibration points measured directly after each spectroscopy point. To account for the Zeeman shift, the atoms are alternately excited from the $m_J=+1$ and $m_J=-1$ states. The red line is a fit of two Gaussians showing typical widths of about 10 kHz.

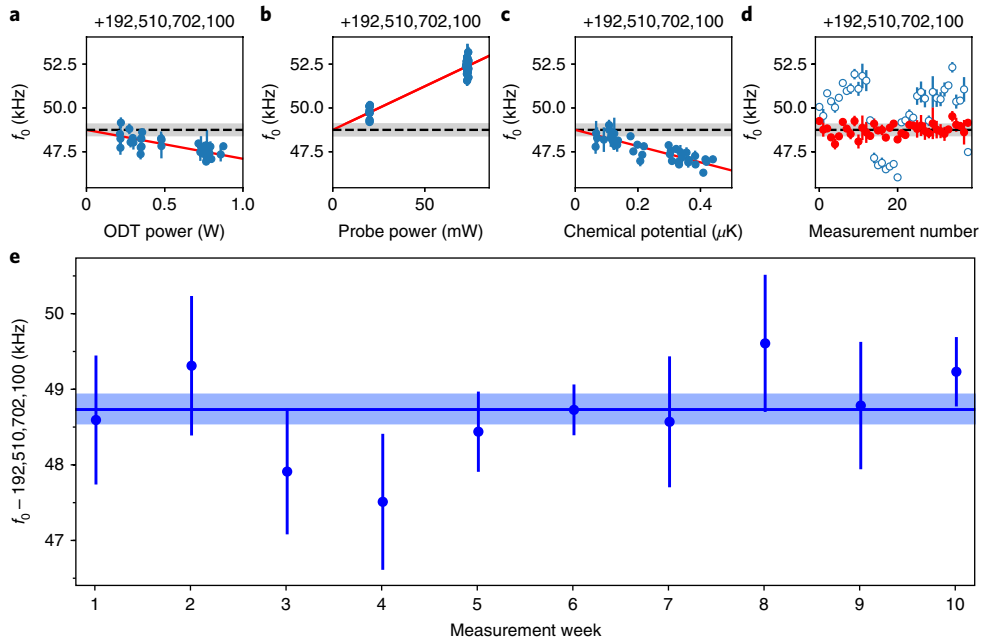

Fig. 3 | Transition frequency measurement. a–d, Results of a multiple regression fit (red lines) to a single dataset. **a–c**, Partial residual plots for each of the fit parameters, error bars are 1 standard deviation from a Gaussian fit. **d**, Measured frequencies (blue open circles) and the residuals with corresponding errors of the regression model (red circles). The grey band in all these figures indicates the 1σ uncertainty on the transition frequency (black dashed line) determined from this particular dataset. **e**, Measured transition frequency per measurement week, error bars are systematic errors. The data point at week six is derived from the multiple regression fit shown in **a–d**, and the other points are based on similar data sets. The blue line and blue band indicate the weighted average and 1σ uncertainty.

number of atoms at high density. To break this correlation as much as possible, we varied the chemical potential of the BEC while keeping the ODT power fixed. This was achieved by varying the hold time in the ODT before applying probe light between 200 ms and a few seconds. Due to the fairly short (~2 s, limited by off-resonant scattering of the ODT light) one-body lifetime of the BEC in the ODT, this allows for significant modification of the size of the BEC.

Magic wavelength. The determination of the magic wavelength was performed over two measurement campaigns: a first 'coarse' campaign, and a second 'high-resolution' campaign during which the absolute transition frequency was also measured. The results from the coarse campaign are shown in Fig. 4a,b, along with the predicted range from calculations[31]. These measurements gave a first estimate of the magic wavelength. However, during this first campaign the mean-field shift was not corrected for, leading to a small systematic offset on the magic wavelength.

During the final measurement campaign, the ODT laser wavelength was varied over a smaller range to more precisely pinpoint the magic wavelength. Figure 4c shows the results from this campaign. To determine the magic wavelength we compare these data to the calculated polarizability curves[31]. The dominant uncertainty in these calculations depends only very weakly on wavelength and appears as a constant offset. The calculated polarizability can be related directly to the measured Stark shift by a scaling factor that corrects for the laser intensity (see Methods). By fitting the data to the calculated polarizability with a constant offset and a scaling factor, we also account for the slight curvature of the polarizability curve over the measured wavelength range. From this fit we then extract the laser intensity, a constant offset correction to the calculated polarizability and the zero-crossing. We find the light intensity at the centre of the trap to be $1.0(1)\times10^8\,\mathrm{W\,m^{-2}}$ (numbers in parenthesis are 1σ uncertainties in the last digits) using a 1 W ODT beam. This intensity is roughly half of our estimate assuming perfect focusing conditions and beam quality[44]. The constant offset correction to the polarizability is found to be 3.4(5) a_0^3. The zero crossing of the fitted curve corresponds to the magic wavelength and is found at 319.81592(15) nm, which is in good agreement with the calculated values of 319.815(3) nm (ref. [31]) and 319.81607(9) nm (ref. [38]). The vector and tensor parts of the polarizability are negligible at the current level of uncertainty (see Supplementary Material) and also do not influence the measurement of the transition frequency.

Mean-field shift and scattering length. The excited $2\,^1S_0$ atoms experience a different mean-field potential compared to the remaining $2\,^3S_1$ atoms because of the difference in scattering length. This leads to a shift of the transition frequency known as the mean-field, or cold-collision shift[40]. The full-width of the mean-field lineshape[41] $S(\nu)$ turns out to be small compared to the observed linewidth. At the maximum density used in the experiments (peak density $n(0)\approx4.5\times10^{13}\,\mathrm{cm^{-3}}$ or equivalently $\mu\approx k_\mathrm{B}\times0.5\,\mu\mathrm{K}$, where k_B is the Boltzmann constant), a full width $\delta\nu_{\max}\approx4.4\,\mathrm{kHz}$ is expected (see Supplementary Material). The additional a.c. Stark shift contribution to the width[42] is negligible for the range of ODT laser wavelengths used in the final measurement campaign. Possible line-pulling effects due to the asymmetric lineshape were investigated by fitting Gaussians to simulations of the broadened lineshape, but were not found to affect the fitted frequencies.

The only observable effect of the mean-field interaction is therefore the average shift of this lineshape. We derive this average shift analytically by integrating the shift over the lineshape (see Supplementary Material for a detailed derivation):

$$\langle\Delta\nu_{\mathrm{MFS}}\rangle=\frac{\int\nu S(\nu)\mathrm{d}\nu}{\int S(\nu)\mathrm{d}\nu}=\frac{4}{7h}\left(\frac{a_{\mathrm{tt}}-a_{\mathrm{ts}}}{a_{\mathrm{tt}}}\right)\mu \qquad (1)$$

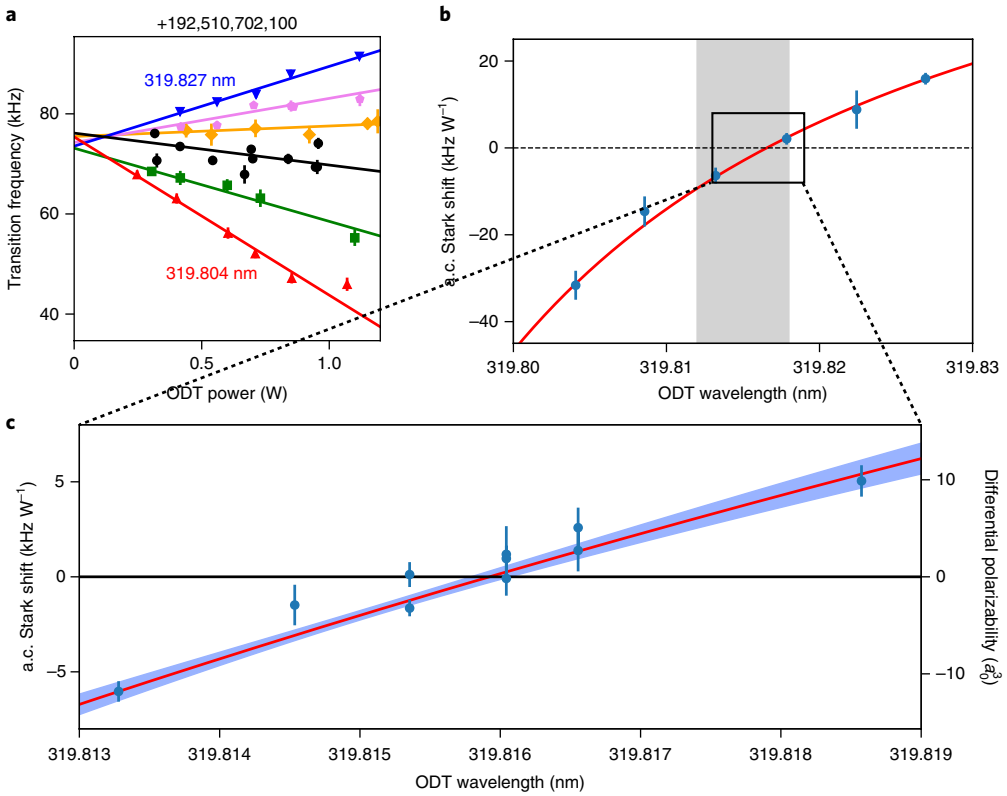

Fig. 4 | Determination of the magic wavelength. a, Transition frequency, including standard deviation to a Gaussian fit, as a function of laser power for several wavelengths (coloured data points), showing only the 'Coarse' scan, with a linear fit at each wavelength (coloured lines) to determine the a.c. Stark shift. **b**, Slopes of the fitted lines in **a**, with 1σ error bars, as a function of the ODT laser wavelength. The grey region indicates the predicted range for the magic wavelength[31]. **c**, 'Fine' scan of the a.c. Stark shift with the ODT power regression results and 1σ error bars. The red line represents a fit of the polarizability curve from ref. [31], with the blue region showing the 1σ uncertainty on this fit. The magic wavelength condition is found at the zero-crossing.

where a_{tt} and a_{ts} are the scattering lengths for triplet–triplet and triplet–singlet collisions, respectively, h is the Planck constant and μ is the chemical potential of the BEC.

The mean-field shift slope was found by including a linear regression to the chemical potential of the BEC in the multiple regression model shown in Fig. 3c. Averaging over all measurements, we find a slope of $-5.0(4)\,\mathrm{kHz\,\mu K^{-1}}$. By rewriting equation (1) we can express the unknown triplet–singlet scattering length in units of the very well known triplet–triplet scattering length, $a_{tt} = +7.512(5)\,\mathrm{nm} = +142.0(1)\,a_0$ (ref. [45]). We find $a_{ts} = +82.5(5.2)\,a_0$, which is in agreement with our previous result[42] of $a_{ts} = +50(10)_{stat}(43)_{syst}\,a_0$.

Transition frequency. The final measured transition frequency is corrected for a number of systematic shifts, as shown in Table 1. By far the largest of these is the recoil shift correction due to the absorption of a 1,557 nm photon, $\Delta f_{rec} = -h/(2m\lambda^2) = -20.554\,\mathrm{kHz}$, with negligible uncertainty.

Another systematic effect affecting all measurements equally is the frequency offset of the Cs clock with respect to the International System of Units (SI) second, to which all measurements are referenced. By comparing the clock with Global Positioning System (GPS) time over the course of the entire measurement campaign, a fractional frequency offset of $-1.9(2)\times10^{-13}$ was found (see Methods). By correcting for this offset, the clock was calibrated to within its specified stability floor of 5×10^{-14}, which contributes to the error budget. The measured transition frequency was corrected for the clock offset, corresponding to −36 Hz on the optical frequency.

Table 1 | Measured $2\,^3S_1 \rightarrow 2\,^1S_0$ transition frequency along with corrections and comparison to several alternative determinations

Term	Correction (kHz)	Uncertainty (kHz)
Measured frequency	192,510,702,169.31	-
Recoil shift	−20.554	-
a.c. Stark shift (probe)		
a.c. Stark shift (ODT)		} 0.192*
Mean-field shift		
Statistical	-	0.032
Cs clock	−0.036	0.010
Black-body radiation shift	<0.005	-
d.c. Stark shift	<0.001	-
Doppler shift	$<10^{-4}$	-
Quantum interference	$<10^{-4}$	-
Second-order Zeeman	$<10^{-5}$	-
Total	**192,510,702,148.72**	**0.20**
van Rooij et al.[29]	192,510,702,145.6	1.8
IE($2\,^3S_1$) - IE($2\,^1S_0$)[18–20,47]	192,510,702,156	42
Pachucki et al.[2] (theory)	192,510,703,400	800

IE, ionization energy. *Uncertainty is correlated in the multiple regression model

Additional systematics are the black-body radiation shift, a d.c. Stark shift due to the ion-MCP bias voltage, a Doppler shift from laser-induced drift of the BEC, possible shifts due to quantum interference with far-off resonant transitions[24] and the second-order Zeeman shift. None of these contribute significantly to the final error budget, and could be neglected in the final result. Details of these estimations can be found in the Supplementary Material.

Figure 3e shows the weekly average of all frequency measurements corrected for the systematic effects identified. The statistical error on the field-free transition frequency as determined by the multiple regression fits is large compared to the systematic error, and remains as the dominant contribution to the error budget after averaging over all results, as shown in Table 1. Finally, we determine the $2\,^3S_1 \rightarrow 2\,^1S_0$ transition frequency to be 192,510,702,148.72(20) kHz, which corresponds to a relative uncertainty $\delta\nu/\nu = 1.0 \times 10^{-12}$.

Discussion and conclusion

The magic wavelength found in this work is in very good agreement with our earlier calculation[31] but is more accurate by over an order of magnitude. Very recent full-configuration-interaction calculations incorporating relativistic and recoil effects give the magic wavelength as 319.816 07(9) nm, which is of a similar accuracy to our measurement and in excellent agreement[38]. It is interesting to make the comparison with measurements on the tune-out wavelength (the wavelength for which the polarizability vanishes) for the $2\,^3S_1$ level at 413 nm[37]. Here a discrepancy with high-precision calculations was found that was attributed to QED effects[36], indicating that measurements of atomic polarizablity can be used as an alternative means of testing QED.

The triplet–singlet scattering length a_{ts} derived from the mean-field shift measured in this work is more accurate than the previous experimental bound[42] by an order of magnitude, and in good agreement. This value can be used to test quantum chemistry calculations of the relevant molecular potentials. Interestingly, a previously reported estimate[42], derived from ab-initio calculations of the $1^3\Sigma_g^+$ and $2^3\Sigma_g^+$ molecular potentials[46], found $a_{ts} = +42^{+0.5}_{-2.5} a_0$, which disagrees significantly with the value of $a_{ts} = +82.5(5.2)\ a_0$ found in this work. This discrepancy may be related to the high ionization cross-section, which causes the complex optical potential method used in these calculations to break down.

The $2\,^3S_1 \rightarrow 2\,^1S_0$ transition frequency obtained in this work improves the earlier measurement by van Rooij et al.[29] by an order of magnitude. The results differ by 1.7σ (see Table 1). This difference may be due to a slight underestimation of the mean-field shift in that work, which was reported as 0.1(1.1) kHz. Based on the slope of the mean-field shift found in this work and a rough estimation of the chemical potentials used in ref. [29], we estimate that the mean-field shift in that work may have been slightly larger, which would require a correction of the previously measured transition frequency of about +2 kHz, reducing the difference between both results to within 1σ.

We can test for consistency with other experiments by taking the difference in ionization energy between the $2\,^3S_1$ and $2\,^1S_0$ levels. These ionization energies can be determined from transition frequency measurements[18–20] and the theoretical ionization energy of the $3\,^{1,3}D$ levels[47] which can be calculated to high accuracy. As shown in Table 1, the measured transition frequency is in excellent agreement with this difference, although more accurate by more than two orders of magnitude. The measured transition frequency is also in reasonable agreement (1.6σ) with a direct QED calculation[2], although the estimated uncertainty in this calculation is several orders of magnitude larger (see Table 1). This uncertainty is currently of the same order as the total nuclear size shift, but is anticipated to be reduced[2], which would allow a direct determination of the ^{4}He nuclear charge radius from the measured transition frequency.

At the current state of the theory, nuclear size information can still be derived at high accuracy by looking at the ^{3}He–^{4}He isotope shift on this transition, for which the estimated uncertainty in the calculations is much smaller (0.19 kHz)[2]. Taking the difference between the transition frequency measured in this work and the $2\,^3S_{1,F=3/2} \rightarrow 2\,^1S_{0,F=1/2}$ transition frequency in ^{3}He (ref. [29]), we derive an updated value of the differential nuclear charge radius $\delta r^2 = r^2(^3\mathrm{He}) - r^2(^4\mathrm{He}) = 1.041(7)\ \mathrm{fm}^2$ (see ref. [2] for details of the calculation), where the error is now dominated by the 1.5 kHz accuracy on the ^{3}He transition frequency. This new value agrees with electron scattering[30] ($\delta r^2 = 1.066 \pm 0.06\ \mathrm{fm}^2$) but still disagrees with determinations based on the $2\ ^3S_1 \rightarrow 2\ ^3P_{0,1,2}$ transitions[27,28]. The very recent measurement[19] of the $2\,^3S_1 \rightarrow 2\,^3P_1$ transition frequency in ^{4}He showed a 20σ discrepancy with respect to ref. [28], which also indicates the need for further investigation of that transition. In the immediate future, we aim to improve the measurement of the $2\,^3S_{1,F=3/2} \rightarrow 2\,^1S_{0,F=1/2}$ transition in ^{3}He, which may bring the uncertainty on δr^2 down to $<0.002\ \mathrm{fm}^2$. This is actually better than the expected accuracy from muonic helium, which will be limited to $0.0031\ \mathrm{fm}^2$ because of theoretical uncertainty in calculating the nuclear-structure two-photon exchange contribution to the Lamb shift[48].

The measurements presented in this work advance our knowledge of the helium atom in several ways. The $2\,^3S_1 \rightarrow 2\,^1S_0$ transition frequency is measured to be 192,510,702,148.72(20) kHz, intimately tying the ortho- and parastates together and allowing us to extract the ^{3}He–^{4}He nuclear charge radius difference with improved accuracy. The magic wavelength on this transition is determined to be 319.81592(15) nm, in good agreement with calculations, and provides a stringent test for precision calculations of polarizabilities. Finally, the measurement of the mean-field shift allows extraction of the $2\,^3S_1 - 2\,^1S_0$ scattering length as $+82.5(5.2)a_0$, which disagrees with recent quantum-chemistry calculations.

Methods

Methods, including statements of data availability and any associated accession codes and references, are available at https://doi.org/10.1038/s41567-018-0242-5.

Received: 5 April 2018; Accepted: 5 July 2018;
Published online: 13 August 2018

References

1. Parthey, C. G. et al. Improved measurement of the hydrogen 1*S*–2*S* transition frequency. *Phys. Rev. Lett.* **107**, 203001 (2011).
2. Pachucki, K., Patkóš, V. & Yerokhin, V. A. Testing fundamental interactions on the helium atom. *Phys. Rev. A.* **92**, 062510 (2017).
3. Mohr, P. J., Taylor, B. N. & Newell, D. B. CODATA recommended values of the fundamental physical constants: 2014. *Rev. Mod. Phys.* **88**, 035009 (2016).
4. Hanneke, D., Fogwell, S. & Gabrielse, G. New measurement of the electron magnetic moment and the fine structure constant. *Phys. Rev. Lett.* **100**, 120801 (2008).
5. Biraben, F. Spectroscopy of atomic hydrogen. How is the Rydberg constant determined? *Eur. Phys. J. Spec. Top.* **172**, 109–119 (2009).
6. Sturm, S. et al. High-precision measurement of the atomic mass of the electron. *Nature* **506**, 467–470 (2014).
7. Pohl, R. et al. The size of the proton. *Nature* **466**, 213–216 (2010).
8. Antognini, A. et al. Proton structure from the measurement of 2*S*–2*P* transition frequencies of muonic hydrogen. *Science* **339**, 417–420 (2013).
9. Beyer, A. et al. The Rydberg constant and proton size from atomic hydrogen. *Science* **358**, 79–85 (2017).
10. Fleurbaey, H. et al. New measurement of the 1*S*–3*S* transition frequency of hydrogen: contribution to the proton charge radius puzzle. *Phys. Rev. Lett.* **120**, 183001 (2018).
11. Pohl, R. et al. Laser spectroscopy of muonic deuterium. *Science* **353**, 669–673 (2016).
12. Nebel, T. et al. The Lamb-shift experiment in muonic helium. *Hyperfine Interact.* **212**, 195–201 (2012).
13. Kandula, D. Z., Gohle, C., Pinkert, T. J., Ubachs, W. M. G. & Eikema, K. S. E. Extreme ultraviolet frequency comb metrology. *Phys. Rev. Lett.* **105**, 063001 (2010).

14. Hodgman, S. S. et al. Metastable helium: A new determination of the longest atomic excited-state lifetime. *Phys. Rev. Lett.* **103**, 053002 (2009).
15. Cancio Pastor, P. et al. Absolute frequency measurements of the 2 $^3S_1 \rightarrow 2\ ^3P_{0,1,2}$ atomic helium transitions around 1083 nm. *Phys. Rev. Lett.* **92**, 023001 (2004).
16. Luo, P.-L., Peng, J.-L., Shy, J.-L. & Wang, L.-B. Precision frequency metrology of helium 2 $^1S_0 \rightarrow 2\ ^1P_1$ transition. *Phys. Rev. Lett.* **111**, 013002 (2013).
17. Notermans, R. P. M. J. W. & Vassen, W. High-precision spectroscopy of the forbidden 2 $^3S_1 \rightarrow 2\ ^1P_1$ transition in quantum degenerate metastable helium. *Phys. Rev. Lett.* **112**, 253002 (2014).
18. Luo, P.-L. et al. Precision frequency measurements of ^{3,4}He 2 $^3P \rightarrow 3\ ^3D$ transitions at 588 nm. *Phys. Rev. A.* **94**, 062507 (2016).
19. Zheng, X. et al. Measurement of the frequency of the 2 ^3S–2 ^3P transition of ^{4}He. *Phys. Rev. Lett.* **119**, 263002 (2017).
20. Huang, Y.-J. et al. Frequency measurement of the 2 $^1S_0$–3 $^1D_2$ two-photon transition in atomic ^{4}He. *Phys. Rev. A.* **97**, 032516 (2018).
21. Borbely, J. S. et al. Separated oscillatory-field microwave measurement of the 2 $^3P_1$–2 $^3P_2$ fine-structure interval of atomic helium. *Phys. Rev. A.* **79**, 060503(R) (2009).
22. Smiciklas, M. & Shiner, D. Determination of the fine structure constant using helium fine structure. *Phys. Rev. Lett.* **105**, 123001 (2010).
23. Zheng, X. et al. Laser spectroscopy of the fine-structure splitting in the 2 ^3P_J levels of ^{4}He. *Phys. Rev. Lett.* **118**, 063001 (2017).
24. Marsman, A., Horbatsch, M. & Hessels, E. A. Quantum interference effects in saturated absorption spectroscopy of $n=2$ triplet helium fine structure. *Phys. Rev. A.* **91**, 062506 (2015).
25. Wang, L.-B. et al. Laser spectroscopic determination of the ^{6}He nuclear charge radius. *Phys. Rev. Lett.* **93**, 142501 (2004).
26. Mueller, P. et al. Nuclear charge radius of ^{8}He. *Phys. Rev. Lett.* **99**, 252501 (2007).
27. Shiner, D., Dixson, R. & Vedantham, V. Three-nucleon charge radius: A precise laser determination using ^{3}He. *Phys. Rev. Lett.* **74**, 3553–3556 (1995).
28. Cancio Pastor, P. et al. Frequency metrology of helium around 1083 nm and determination of the nuclear charge radius. *Phys. Rev. Lett.* **108**, 143001 (2012).
29. van Rooij, R. et al. Frequency metrology in quantum degenerate helium: Direct measurement of the 2 $^3S_1 \rightarrow 2\ ^1S_0$ transition. *Science* **333**, 196–198 (2011).
30. Sick, I. Zemach moments of ^{3}He and ^{4}He. *Phys. Rev. C.* **90**, 064002 (2014).
31. Notermans, R. P. M. J. W., Rengelink, R. J., van Leeuwen, K. A. H. & Vassen, W. Magic wavelengths for the 2 $^3S \rightarrow 2\ ^1S$ transition in helium. *Phys. Rev. A.* **90**, 052508 (2014).
32. Campbell, S. L. et al. A Fermi-degenerate three-dimensional optical lattice clock. *Science* **358**, 90–94 (2017).
33. Marti, G. E. et al. Imaging optical frequencies with 100 μHz precision and 1.1 μm resolution. *Phys. Rev. Lett.* **120**, 103201 (2018).
34. Ludlow, A., Boyd, M. M., Ye, J., Peik, E. & Schmidt, P. Optical atomic clocks. *Rev. Mod. Phys.* **87**, 637–701 (2015).
35. Mitroy, J. & Tang, L.-Y. Tune-out wavelengths for metastable helium. *Phys. Rev. A.* **88**, 052515 (2013).
36. Zhang, Y.-H., Tang, L.-Y., Zhang, X.-Z. & Shi, T.-Y. Tune-out wavelength around 413 nm for the helium 2 $^3S_1$ state including relativistic and finite-nuclear-mass corrections. *Phys. Rev. A.* **93**, 052516 (2016).
37. Henson, B. M. et al. Precision measurement for metastable helium atoms of the 413 nm tune-out wavelength at which the atomic polarizability vanishes. *Phys. Rev. Lett.* **115**, 043004 (2015).
38. Wu, F.-F. et al. Relativistic full-configuration-interaction calculations of magic wavelengths for the 2 $^3S_1 \rightarrow 2\ ^1S_0$ transition of helium isotopes. Preprint at https://arXiv.org/abs/1804.01218 (2018).
39. Fried, D. G. et al. Bose–Einstein condensation of atomic hydrogen. *Phys. Rev. Lett.* **81**, 3811–3814 (1998).
40. Killian, T. C. et al. Cold collision frequency shift of the 1*S*–2*S* transition in hydrogen. *Phys. Rev. Lett.* **81**, 3807–3810 (1998).
41. Killian, T. C. 1*S*–2*S* spectrum of a hydrogen Bose–Einstein condensate. *Phys. Rev. A.* **61**, 033611 (2000).
42. Notermans, R. P. M. J. W., Rengelink, R. J. & Vassen, W. Comparison of spectral linewidths for quantum degenerate bosons and fermions. *Phys. Rev. Lett.* **117**, 213001 (2016).
43. Vassen, W. et al. Cold and trapped metastable noble gases. *Rev. Mod. Phys.* **84**, 175–210 (2012).
44. Rengelink, R. J., Notermans, R. P. M. J. W. & Vassen, W. A simple 2 W continuous-wave laser system for trapping ultracold metastable helium atoms at the 319.8 nm magic wavelength. *Appl. Phys. B* **122**, 122 (2016).
45. Moal, S. et al. Accurate determination of the scattering length of metastable helium atoms using dark resonances between atoms and exotic molecules. *Phys. Rev. Lett.* **96**, 023203 (2006).
46. Müller, M. W. et al. Experimental and theoretical studies of the Bi-excited collision systems He* (2 ^3S) + He*(2 ^3S, 2 ^1S) at thermal and subthermal kinetic energies. *Z. Phys. D* **21**, 89–112 (1991).
47. Morton, D. C., Wu, Q. & Drake, G. W. F. Energy levels for the stable isotopes of atomic helium (^{4}He I and ^{3}He I). *Can. J. Phys.* **84**, 83–105 (2006).
48. Diepold, M. et al. Theory of the Lamb shift and fine structure in muonic ^{4}He ions and the muonic ^{3}He–^{4}He isotope shift. Preprint at https://arXiv.org/abs/1606.05231v2 (2017).

Acknowledgements

We would like to thank R. van der Beek for useful discussions and a critical reading of the manuscript, D. Cocks and I. Whittingham for helpful discussions, and R. Kortekaas for technical support. We gratefully acknowledge financial support from the Netherlands Organisation for Scientific Research (NWO).

Author contributions

R.J.R. and R.P.M.J.W.N. constructed the experimental set-up. R.J.R., Y.v.d.W. and M.D.H. performed the measurements. R.J.R., Y.v.d.W. and R.J. investigated systematic effects. R.J.R. performed the data analysis. R.J.R., R.P.M.J.W.N. and K.S.E.E. performed and discussed the frequency metrology. W.V. initiated and supervised the project. All authors discussed the results and contributed to the manuscript.

Competing interests

The authors declare no competing interests.

Additional information

Supplementary information is available for this paper at https://doi.org/10.1038/s41567-018-0242-5.

Reprints and permissions information is available at www.nature.com/reprints.

Correspondence and requests for materials should be addressed to W.V.

Publisher's note: Springer Nature remains neutral with regard to jurisdictional claims in published maps and institutional affiliations.

Methods

Experimental sequence. The tightly focused (waist <100 μm) ODT beams trap the atoms in a cigar-shaped harmonic potential. At 1 W input power, typical trap frequencies are $\omega_{ax} \approx 2\pi \times 35$ Hz in the axial direction and $\omega_{rad} \approx 2\pi \times 300$ Hz in the radial direction. The probe laser beam has an input power of up to 80 mW and a larger beam waist (~300 μm) to ensure uniform illumination. We align the probe beam by overlapping it with the incident ODT beam. The polarization of the probe beam is linear, but the direction is rotated with a motorized rotation stage to optimize the ion signal depending on whether the transition is made from the $m_J=+1$ or the $m_J=-1$ state.

In the ODT, probe light is applied for about 100 ms, after which the remaining atoms are released to fall under gravity onto the MCP detector. This excitation time is chosen to yield sufficient signal while being short enough to not alter the chemical potential of the BEC by more than a few per cent. During this step, the excited $2\,^1S_0$ atoms collide with the remaining $2\,^3S_1$ atoms in a strongly Penning-ionizing collision channel. We expect an ionization rate comparable to that of unpolarized $2\,^3S_1$ atoms, corresponding to a lifetime of about 1 ms for the $2\,^1S_0$ atoms. The He^+ ions produced by this process are detected by a second MCP detector (the ion-MCP) biased at −2.5 kV and located 11 cm above the trap. The signal from the ion-MCP is amplified by a pulse amplifier/discriminator and passed into a counter to yield the spectroscopy signal. Based on an excitation fraction of ~5%, and a peak signal height of a few thousand counts from a BEC of a few million atoms, we estimate a detection efficiency of ~2%. We attribute the low efficiency to shielding of the trap volume by the grounded re-entrant windows.

To mitigate the Zeeman shift, we alternate between exciting from the $m_J=+1$ and $m_J=-1$ states. We transfer the atoms from the $m_J=+1$ to the $m_J=-1$ state via a Landau–Zener sweep that consists of a magnetic field ramp while radiofrequency-coupling between the magnetic substates is applied[49]. After application of the probe light a second sweep brings the $m_J=-1$ atoms back to the $m=+1$ state so that the time of flight is not affected. In the case of $m_J=+1$ atoms the same sweep is performed without the radiofrequency-coupling to make sure no systematic magnetic field difference is introduced. After every measurement an identical measurement is performed with the probe light blocked to calibrate the level of background ion counts. We attribute this background to ionization of background gas by the 320 nm ODT light. This is corroborated by the fact that the background count rate is linearly proportional to the ODT laser power and increases when the background pressure is increased by temporarily closing the safety valve going to the turbopump of the main chamber.

We estimate the linewidth of the probe laser as approximately 5 kHz, based on the combined effects of residual frequency comb noise, electronic noise on the phase-locked loop, and the 60-m-long uncompensated fibre link between the frequency comb and the set-up. However, the observed lineshapes are broader, showing approximately Gaussian profiles of about 10 kHz in width. We attribute the additional broadening to a small residual oscillation of the BEC inside the trap that causes Doppler broadening. Absorption images of the expanding BEC indeed show random velocity fluctuations with a standard deviation of about 3–4 mm s^{-1} in the axial direction. A simple model of a damped harmonic oscillator driven by statistical fluctuations of the axial trap position can quantitatively explain these observations.

Polarizability and a.c. Stark shift. The main uncertainty in the calculations of ref. [31] is due to approximations made in estimating the contribution to the polarizability due to coupling to the ionization continuum. Since this contribution is far off-resonant, we can neglect its wavelength dependence and treat it as a d.c. offset. The calculated polarizabilities are given in atomic units (a.u.), which can be converted into the SI units using $[1a_0^3]_{a.u.}=[4\pi\epsilon_0 a_0^3]_{SI} \approx 1.64877\times10^{-41}\,\mathrm{J\,V^{-2}\,m^2}$. The intensity of the laser beam can now be calculated from the scale of the polarizability compared to the a.c. Stark shift using $I=2\epsilon_0 ch\Delta\nu/\mathrm{Re}(\Delta\alpha)$, where ϵ_0 is the permittivity of free space, c the speed of light, h Planck's constant, $\Delta\alpha$ the differential polarizability and $\Delta\nu$ the observed a.c. Stark shift[50].

Absolute frequency determination. The ODT laser wavelength is derived from both the spectroscopy laser and a second free-running fibre laser. Because the spectroscopy laser frequency is determined with much higher accuracy, the uncertainty on the ODT laser wavelength is dominated by the free-running laser. This wavelength is measured continuously during the course of the experiment using a high-resolution wavemeter (High Finesse WSU-30) with a specified accuracy of 30 MHz, which was periodically calibrated on the $2\,^3S_1 \rightarrow 2\,^3P_2$ line at 1,083 nm. The laser wavelength was manually adjusted using the temperature control whenever it drifted by more than 50 MHz from the wavelength setpoint for that measurement week.

The spectroscopy laser is locked to an ultrastable laser at 1,542 nm (Menlo Systems) via an optical frequency comb to bridge the wavelength gap in a transfer-lock configuration[42]. The ultrastable laser serves as stable short-term flywheel oscillator for the measurement. Over the course of a measurement day, the frequency of this reference is measured with respect to the Cs clock.

To reconstruct the absolute frequencies of the lasers several beat notes are continuously measured with a zero-dead-time frequency counter, referenced to the Cs clock. The frequencies which are measured are the frequency comb carrier offset frequency, the down-mixed pulse repetition rate, the spectroscopy laser beat note (before mixing in the DDS), and either the virtual beat note or the ultrastable laser beat note. The wavelengths of the lasers were measured using a wavemeter with sufficient resolution to determine the comb mode number of the observed beat notes.

From these data the ultrastable laser frequency was reconstructed, and a linear fit allows us to compensate for the slow drift of this laser during the day. This drift was found to be 22(2) mHz s^{-1} ($1.1(1)\times10^{-16}$ s^{-1}) on average and fluctuating from day to day with a standard deviation of 9 mHz s^{-1}. The modified Allan deviation of these data agrees well with the specified stability of the Cs clock at the measured timescales, typically reaching a stability in the low-10^{-13} region after a single measurement day. In total, the spectroscopy data were acquired over about 30 separate measurement days, yielding in total about 5×10^5 s of total integration time, which is enough to reach the clock's stability floor of 5×10^{-14}.

During the full measurement campaign the time delay between the Cs clock and GPS pulse per second signal was continuously measured. The Allan deviation of this delay averages down with time as τ^{-1}, and catches up with the Cs clock stability after about 10^6 s. Integrating over the full course of the measurement campaign, which took several months (~8×10^6 s), we observed a fractional frequency drift of $-1.9(2)\times10^{-13}$, with an accuracy that exceeds the specified Cs clock stability. We corrected for this drift in the frequency measurement data, but take the specified clock stability floor as a conservative estimate of the uncertainty. The deviations between the GPS disseminated second with respect to the SI definition as reported in the BIPM 'circular T' bulletin[51] were found to be negligible at the current level of uncertainty.

Data processing and statistical analysis. The measured transition frequency data are fitted with a weighted linear least squares model regressing to the ODT and probe laser powers (measured before and after each scan) and the chemical potential of the BEC (as determined from the MCP time-of-flight profile). To separate the purely statistical error from the error due to the systematic shifts, we calculate the point of minimum uncertainty from the covariance matrix of the fit. At this point the uncertainty on the transition frequency is not correlated with the uncertainty in the other parameters and can be considered purely statistical, amounting to 32 Hz. Extrapolating from this point to zero laser power and chemical potential is associated with a systematic uncertainty of 192 Hz, which constitutes the bulk of the uncertainty in this work.

Data availability. Experimental data are available from the corresponding author upon reasonable request.

References

49. Borbely, J. S., van Rooij, R., Knoop, S. & Vassen, W. Magnetic-field-dependent trap loss of ultracold metastable helium. *Phys. Rev. A.* **85**, 022706 (2012).
50. Grimm, R., Weidemüller, M. & Ovchinnikov, Y. B. Optical dipole traps for neutral atoms. *Adv. At. Mol. Opt. Phys.* **42**, 95–170 (2000).
51. Circular T bulletins 358–360 *BIPM* https://www.bipm.org/en/bipm-services/timescales/time-ftp/Circular-T.html (2017).